Characterising 3D Force Sensors to Study Cellular Forces in Tissues

THESIS

submitted in partial fulfillment of the
requirements for the degree of

MASTER OF SCIENCE
in
PHYSICS

Author :	Aditya Aniruddha Sane
Student ID :	2506874
Supervisor :	Prof.Dr. Thomas Schmidt
2^{nd} corrector :	Dr. Alexandre Morin

Leiden, The Netherlands, August 19, 2021

Characterising 3D Force Sensors to Study Cellular Forces in Tissues

Aditya Aniruddha Sane

Huygens-Kamerlingh Onnes Laboratory, Leiden University
P.O. Box 9500, 2300 RA Leiden, The Netherlands

August 19, 2021

Abstract

Mechanical forces regulate many cell functions such as differentiation and proliferation. Existing traction force methodology is often limited to measurements in the two-dimensional plane. Recent studies have used hydrogel micro-particles to measure cell forces in a complex 3D environment such as a spheroid. However, these micro-particles have not been fully characterised. We show here the synthesis of hydrogel micro particles with size and stiffness similar to cells. We also show that the measured effective Young's modulus is dependent on the size of the particle measured. The softest beads with a Young's modulus of 175 Pa can measure normal stresses down to $\sim$ 7.3 Pa. The synthesised beads can be used to determine cell forces in tissues such a tumour spheroids or can be used to mimic cells in tissue layers.

Contents

Chapter 1

Introduction

Mechanical forces play an important role in cell behaviour. Recent mechanobiology studies have shown mechanical forces are critical in driving cell morphogenesis and stem cell differentiation [1]. Rauzi *et al.* showed that anisotropic forces lead to tissue elongation in Drosophila embryos [2]. Mechanical forces also affect disease progression and are important for cancer cell proliferation. Tse *et al.* showed that generation of compressive stress within tumours on confinement lead to formation of 'leader cells' that facilitate movement and proliferation [3]. A similar result was shown by Mekhdjian *et al.* where stiffer Extracellular Matrix (ECM) stimulated a more invasive phenotype of tumour cells. [4]. Mechanical properties can also be used to monitor pathological and physiological changes in cells without the use of molecular markers [5, 6]. Mechanical forces therefore regulate a varied number of cellular functions and behaviour and it is important to quantify them in order to better understand the phenomena that they govern.

These mechanical forces are measured using various techniques. One of the major methods to quantify cell force is Traction Force Microscopy (TFM). In TFM, cells are seeded in vitro on a substrate embedded with fluorescent beads. When the cells apply forces the deformation of the substrate leads to movement of the fluorescent beads which is tracked to obtain the traction forces. The beads are of the size of micrometers which allows for subcellular resolution when tracking traction forces. High resolution TFM was used to show force fluctuations in cell focal adhesions mediate ECM rigidity sensing by cells which helps in guided cell migration [7]. Another method to probe cell adhesion and forces is by micro pillars. Here, the cells are adhered to microfabricated 3D pillars. The stiffness of the pillars is determined by its height and width. The pillars bend on force applica-

tion and the forces can be calculated based on how the pillars bend. This method has been used to determine contractile forces exerted by cells during adhesion [8, 9]. Other methods include micropipette aspiration where cells are sucked into a pipette causing the cell to form an elongated tether [10]. The suction pressure and the length of the tether formed can be used to determine the force. Atomic force microscopy (AFM) is also a robust method to determine the stiffness and shape of cells by indenting the cells with flexible cantilevers whose deflection is used to determine mechanical properties. These techniques even though well characterised measure forces in 2D plane. Another drawback of these techniques is that all these measurements are done in vitro which may not always be representative of the conditions found in vivo.

Cells in vivo exist in a 3D environment. For measurement of forces in 3D environment only a few methods are available. One such method is the oil droplet method where an oil droplet is used as a force sensor. The deformation in the oil droplet on force application can be converted to applied force based on the geometry of the drop. Campas *et al.* used the oil droplet method to quantify mechanical forces in a living embroynic tissue [11]. However, oil being an incompressible liquid, isotropic compressive forces and shear forces cannot be determined using this method. Microfluidic devices are also used to make elastic gel beads that can quantify shear forces too. Mohagheghian *et al.* created these elastic gel particles to determine average compressive forces in the range of 360 -570 Pa in living cell layers [12]. Vorselen et al. used pressure extrusion of polyacrylamide gel through a porous membrane to create mono-disperse beads to measure subcellular force pattern in phagocytic engulfment by T-cells [13]. Vorselen made beads in the range of 5-15 μm with Young's modulus of 1-5 kPa. While different micro-particles have been used, they have still not been properly characterised. The beads have been proposed to mimic cells in their physical properties, such as size and stiffness, in tissue layers and tumours to study cellular force. However, the beads are either too stiff or too big to mimic cells. The aim of this project is synthesise micro-particles that can mimic cells and to characterise them for their size and stiffness.

Chapter 2

Theory

The stiffness of the soft hydrogel micro-particles was characterised by AFM measurements. This was done by probing the spherical particles with an AFM tip which had a spherical indenter. This required knowledge of the interaction between the indenter and the sphere which is discussed below and was first given by Hertz [14].

2.1 Contact Dynamics and Hertz Model

The Young's Modulus of the bead was determined by indenting the micro-particles with the AFM tip which had a spherical indenter. To obtain the Young's modulus from the force and the indentation depth measured, we apply the Hertz model. Figure 2.1A shows the indentation of the spherical body with a spherical indenter with an indentation depth δ. $\delta + x$ is the apparent indention, where 'x' is the apparent increase in indentation due to the bending of the cantilever. The effect due to bending is corrected to obtain δ. R_I is the radius of the indenter and R_S is the radius of the sample. Similarly, E_S and E_I are the Young's moduli of the sample and the indenter. 'a' is the contact radius upon indentation. The contact radius for an indenter indenting an infinitely extending half space is given by[15]:

$$a = \sqrt{\delta \cdot R_I}\,. \tag{2.1}$$

For a spherical indenter the indentation depth and force as described

by Popov *et al.* are given by [15, 16]:

$$F = E^{\dagger}[\frac{a^2 + R^2}{2} \ln \frac{R + a}{R - a} - aR] \,, \tag{2.2a}$$

$$\delta = \frac{a}{2} \ln \frac{R + a}{R - a} \,, \tag{2.2b}$$

where, $E^{\dagger}$ is the effective Young's modulus and is given by

$$\frac{1}{E^{\dagger}} = \frac{1 - \nu_I^2}{E_I} + \frac{1 - \nu_S^2}{E_S} \,, \tag{2.3}$$

where, ν_I and ν_S are the Poisson ratio of the indenter and the sample.
The Hertz model is applicable only for small indentations (5-10% of the sample height). For the Hertz model to be applicable there are some assumptions that are made:

a) The sample is an isotropic solid in the linear elastic regime. This is achieved through small indentations.

b) The indenter is non deformable which directly implies that $E^{\dagger} \approx \frac{E_S}{1-\nu_S^2}$

c) There are no interactions between the indenter and the sample.

Considering these approximations the expression for force becomes

$$F = \frac{E_S}{1 - \nu_S^2}[\frac{a^2 + R^2}{2} \ln \frac{R + a}{R - a} - aR] \,. \tag{2.4}$$

This equation when simplified and written in terms of the indentation δ and force F gives the Young's modulus as

$$E_S = \frac{3}{4} \frac{F(1 - \nu_S^2)}{\delta^{\frac{3}{2}}} \cdot \frac{1}{\sqrt{R}} \tag{2.5}$$

During AFM measurements, the software calculates Young's modulus based on the assumption that we indent an infinitely extending half space. Then R $\approx$ R_I and yields a resulting Young's modulus E_∞. However, in the case of two spheres touching, the contact radius a is reduced and if one assumes an infinitely extending half space they overestimate the contact

radius and consequently, the pressure and the Young's modulus are underestimated. Therefore for a spherical sample and indenter the effective radius $\frac{1}{R} = \frac{1}{R_S} + \frac{1}{R_I}$ is used.

$$\frac{E_S}{E_\infty} = \sqrt{1 + \frac{R_I}{R_S}}\,. \tag{2.6}$$

The Young's modulus obtained from the AFM software needs to be multiplied with the factor above to yield the effective Young's modulus. Figure 2.1D shows how the ratio changes with the size of the bead for $R_I = 5\,\mu\text{m}$. For large beads the ratio approaches 1 where the indenter approaches an infinitely extending half space.

2.2 Force Indentation Curve

Force indentation curves were obtained by indenting the beads using an AFM. In an AFM setup, there is a laser aligned to the cantilever which is used to indent the sample. As the cantilever is moved into the sample there is a deflection in the cantilever which results in the shift of the laser beam. The AFM measurements yield a plot of the deflection of the cantilever (measured in Volts) versus the height of the cantilever. The deflection in Volts is converted to force. Figure 2.1B shows a typical force indentation curve. The plot shows the portion where the tip approaches the sample (in red) and where it retracts (in blue). The x axis shows the distance from the sample. There is no deflection as the tip approaches the sample. As soon as the tip encounters the sample there is an increase in the deflection of the cantilever and hence the force. Here, we indent the sample by ~ 1 µm. As the tip is retracted the force decreases. Due to adhesion with the sample, the tip remains in contact and is deflected downwards as seen in the dip in the blue curve. Once the retraction force is counteracts the adhesion the tip snaps back to its original position. We fit Equation 2.4 to the approach curve as it does not include the interaction due to adhesion to obtain the Young's modulus.

Version of August 19, 2021– Created August 19, 2021 - 15:19

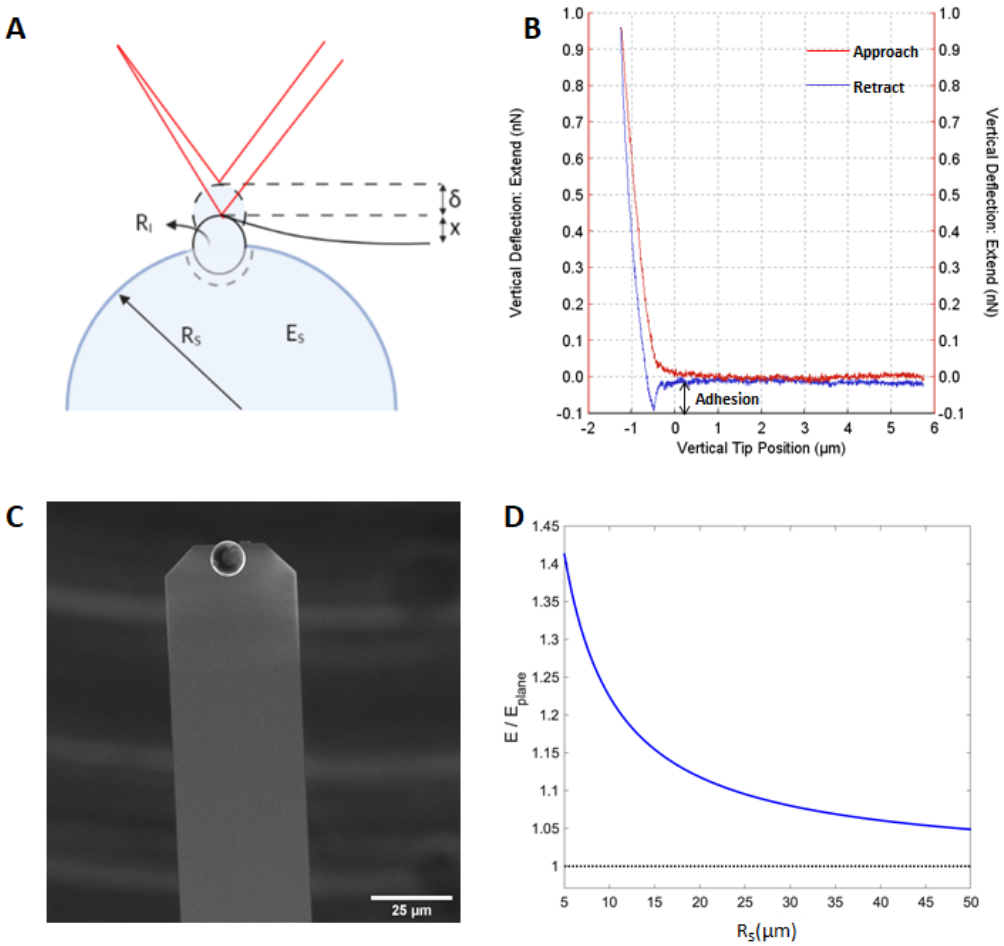

Figure 2.1: Measurement on AFM yields force indentation curves
A) *Schematic of an AFM indentation using a spherical indenter on a spherical sample. The deflection in the cantilever causes a deflection of the laser. The bending of the cantilever (x) is corrected in the analysis software.* ***B)*** *A typical force indentation curve of the tip on 2.3% cross linker sample. When the tip approaches the sample (red), there is no deflection until the tip interacts with the sample and the force increases as indentation increases. During the retraction of the tip (blue) the tip may adhere to the sample causing a dip in the curve.* ***C)*** *Scanning Electron Microscope (SEM) image of the tip used for measurement. The cantilever has a width of 40 µm and the sphere has a diameter of 10 µm* ***D)*** *Ratio of the effective Young's modulus for a spherical bead and Young's modulus for an infinitely extending half space. For large beads the ratio approaches the value for an infinitely extending half space*

Chapter 3

Materials and Methods

In this thesis, we synthesise deformable hydrogel particles using polyacrylamide gel mixture. The particles were fixed to a surface and characterised for stiffness using force spectroscopy measurements on an Atomic Force Microscope (AFM). The sizes distribution for the synthesised particles was determined by analysing Phase Contrast Microscopy images on MATLAB.

3.1 Bead Synthesis

Soft micro particles were synthesised by extrusion of the acrylamide gel into the oil phase through a tubular hydrophobic Shirasu porous glass (SPG) membrane with a height of 20 mm and outer diameter of 10 mm. The membrane had a pore diameter of 3.1 µm. All acrylamide mixtures contained 150 mM NaOH, 0.3% (v/v) tetramethylethylenediamine (TEMED) (Thermo Fisher, 17919), 150 mM MOPS (prepared from MOPS sodium salt with a final pH of 7.4) (Sigma, M9381) along with acrylamide (AAm) (Sigma, A9099), acrylic acid (AAc) (Sigma, 147230) and N,N'-methylenebis acrylamide (BIS) (Sigma, 146072). The final mass concentration of acrylamide components ($C_t = C_{AAc} + C_{AAm} + C_{BIS}$) was 100 mg/mL. The concentration of acrylamide was kept constant at 10% for the cross linker percentage ranging from 1% to 2.3%. We made 12 mL of gel mixture. The membrane was mounted on the internal pressure micro kit extruder (SPG Technology) after being sonicated under vacuum in HPLC grade n-heptane for 5 minutes to remove any trapped gas. The membrane was immersed in the oil phase containing $\sim$ 220 mL hexane ((99% ACS reagent, mixed isomers) (Fisher Science, P216885) and 1% or 3% (v/v) Span80 (Fluka, 85548) as mentioned in the text. The gel was degassed for 15 minutes be-

fore being poured into the module for extrusion. The oil phase was kept under nitrogen atmosphere in a 3-neck water jacketed flask. For extrusion, the pressure of nitrogen in the module was increased step-wise until a continuous flow of beads was seen. This was the critical pressure. The pressure was set at $\sim$ 3 kPa higher than the critical pressure for extrusion. The extrusion took $\sim$ 0.5 to $\sim$3 h. The oil phase was continuously stirred at 350 rpm using a magnetic stirrer. After extrusion, the SPG module was removed and the temperature of the emulsion was increased to 60 °C following which 300 mg of Granular 2,2'-Azobisisobutyronitrile (AIBN) (Sigma, 441090) was added to induce particle polymerisation. The temperature was reduced to 40 °C after 3 h and the emulsion was left as such overnight. The gel was then washed 3$\times$ using hexane and 1$\times$ using 100% ethanol. Between each washing step, the emulsion was centrifuged at 300g for 5 minutes. After the ethanol washing, the beads were dried under nitrogen flow ($\sim$ 2 h). The beads were resuspended in PBS (pH $\sim$ 7.2) overnight and supplemented with 1% (v/v) 0.5 M sodium azide (Sigma, S20002).

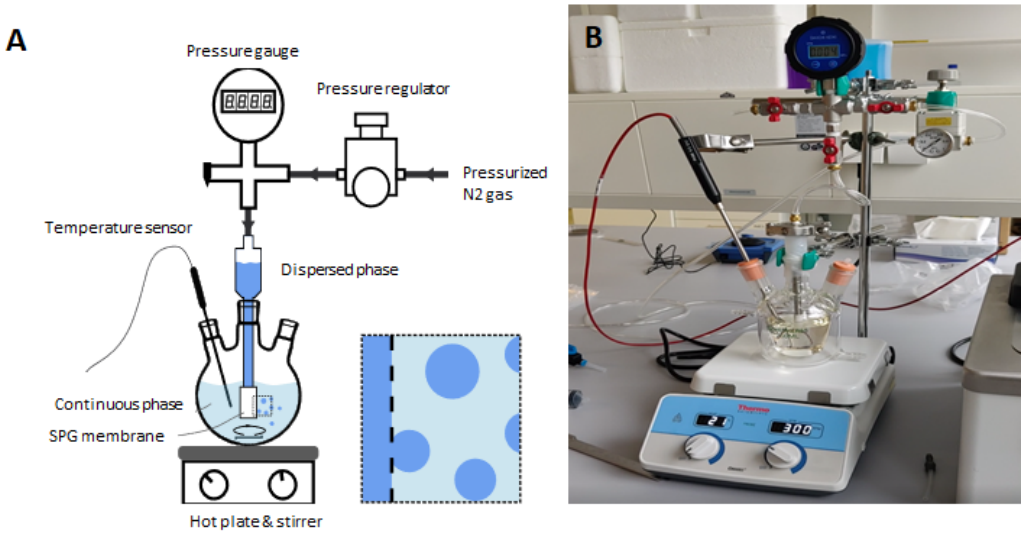

Figure 3.1: Experimental setup for the synthesis of hydrogel micro-particles. ***A)*** *Schematic of the experimental setup used. The gel is is extruded from the membrane (inset) into the continuous phase by applying pressure from the nitrogen gas.* ***B)*** *Actual setup.*

3.2 Bead Immobilization

Bead immobilization was done to fix beads to the petri dish so that they do not move or stick to the AFM cantilever during AFM measurements. The suspended particles were diluted to 15% (v/v) concentration using PBS. 500 µL of diluted particles along with 100 µL 20% (w/v) N -(3 - Dimethylaminopropyl) -N'-ethylcarbodiimide hydrochloride (EDC) (Sigma, E7750) and 100 µL 10% (w/v) N -hydroxysuccinimide (NHS) (Thermo Fisher, 22500) were added in a 60 mm Petri dish and left to incubate for $\sim$ 1.5 h. After incubation, they were washed 3$\times$ with 20 mL PBS and stored again in 5 mL PBS. The measurements were done within one week of fixing the particles.

3.3 Phase Contrast Microscopy

Phase contrast images were taken to determine the size of the beads. Phase Contrast Microscopy was performed using an Axiovert40 (Zeiss) inverted microscope base unit equipped with 10$\times$ NA 0.22 ph1 (Zeiss) objective for phase contrast imaging. The images were captured using a WAT-902H2 Ultimate (CCIR) monochrome CCD camera (WATEC).

3.4 Image Analysis

The images obtained from microscopy (Section 3.3) were post processed in MATLAB to determine the size of the particles. The images were first smoothed using the Gaussian blur filter to remove noise. Then edges were determined using the Canny method [17]. Once the edges were determined, the area detected were filled and filtered based on size to remove small areas. Watershed algorithm was used to find and separate the centres of overlapping beads [18]. Then circles were fit to the areas and circles with eccentricity less than 0.6 were used to determine the size of the beads (Figure 3.2).

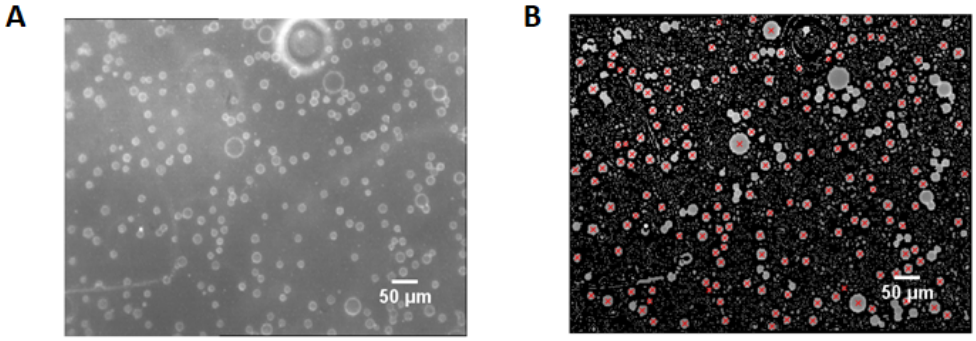

Figure 3.2: Image analysis of beads is used to determine size of the beads. ***A)*** *Original image of the 1.5% cross linker sample 1 using a 10× phase contrast objective.* ***B)*** *Thresholded image shows the detected beads in the image (marked in red). Only those beads whose edge is properly detected are considered.*

3.5 Atomic Force Microscopy

The AFM measurements were performed on immobilized particles (see Section 3.2) using the JPK Nanowizard 4 setup. The tip used had a spherical indenter of radius ~ 5 µm and the cantilever had a spring constant of $\sim 0.15\, N/m$ (NanoAndMore GMBD, CP-qp-CONT-BSG) which was calibrated by thermal tuning before each measurement session (Figure 2.1C). The sample was illuminated from beneath using a LED light source. The tip was centred on the particles and 4-5 nano-indentations were performed on each bead (peak force set point 0.6-0.9 nN) which yielded as many force deformation curves (Figure 2.1B). The data was analysed using the JPK processing software. The force deformation curves were processed by correcting for the offset and drift in the baseline. This was followed by adjusting the contact point to zero and adjusting for the cantilever bending. The Hertz model was then fitted to the corrected curve with the tip radius as 5 µm. The Young's modulus obtained from the fitting was averaged for 4-5 curves obtained for each particle to reduce error. The obtained Young's modulus was corrected using Equation 2.6.

Version of August 19, 2021– Created August 19, 2021 - 15:19

Chapter 4

Results and Discussion

We validated the approach used by Vorselen *et al.* to synthesise soft hydrogel micro-particles. We synthesised micro-particles using a softer gel composition using cross linker concentration of 2.3%, 1.5% and 1%. We obtained the size distribution of the synthesised beads using phase contrast microscopy and image analysis. We obtained the Young's moduli of the beads using AFM measurements.

4.1 Validation of Approach

Before we characterised the hydrogel beads for different cross linker concentrations, we validated the bead synthesis approach as outlined by Vorselen *et al.* [13]. We synthesised beads using 1.5% cross-linker concentration and the acrylic acid concentration was kept at 10%. The span80 concentration was taken to be 3%. The rest of the protocol was followed as outlined in Section 3.1. The size was determined using image analysis and the Young's modulus was determined by fixing the beads and measuring using an AFM. Figure 4.1A (top) shows the size distribution of the synthesised beads. We obtain bead radius of 13 ± 6 μm (mean $\pm$ std.). Figure 4.1A (bottom) shows the measured Young's modulus distribution for 30 beads. The Young's modulus was found to be 4.9 ± 1.4 kPa (mean $\pm$ std.). Within the measurement accuracy, the Young's modulus is in accordance with the expected Young's modulus of ~ 3.5 kPa for 1.5% cross linker percentage as was interpolated from the experimental data shown by Vorselen *et al.* [13]. We also wanted to validate whether the Young's modulus follows the $\frac{1}{\sqrt{R}}$ relation as suggested by Equation 2.5. Figure 4.1B shows the plot for the measured Young's modulus and the measured radius of

the bead. We see that measured beads are in a very small range of 7-10 µm and the Young's modulus shows a no correlation with size with the correlation coefficient of -0.28. The reason we do not observe a correlation of Young's modulus with size of the bead is maybe due to the fact that we probe a very narrow distribution of sizes. Thus, here we show that we can make hydrogel beads with a specific cross linker concentration and the measured Young's modulus agrees well with what is expected from the available literature.

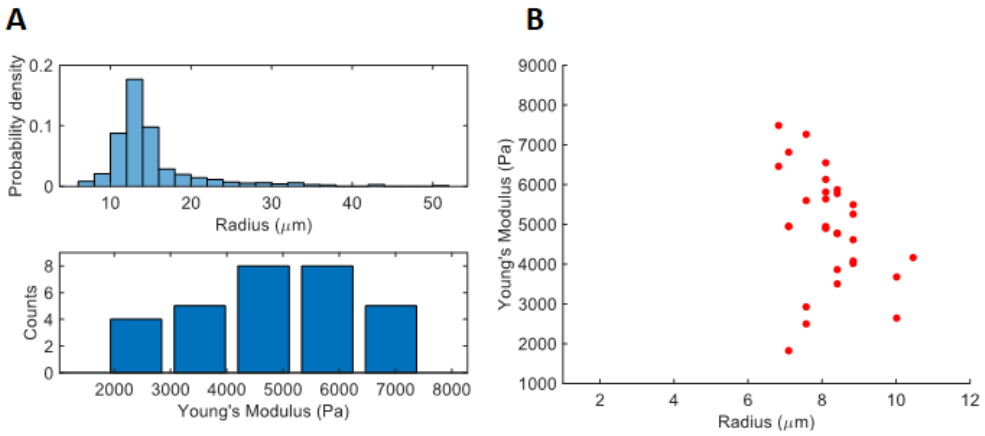

Figure 4.1: Validation of synthesis approach for sample with 1.5% cross linker. ***A)*** *The 1.5% cross linker sample yields a radius of* 13 ± 6 *µm and Young's modulus of* 4.9 ± 1.4 *kPa.* ***B)*** *The Young's modulus shows no correlation with the size of the particle.*

4.2 Size Distribution

After validating the approach we wanted to make softer beads that can mimic cells in their stiffness. For this purpose, we kept the acrylamide concentration at 10% instead of acrylic acid. We synthesised five batches of the particles: two with 2.3%, two with 1.5% and one with 1% cross linker concentration. We characterised these batches for size using image analysis. For the 2.3% sample shown in Figure 4.2A, we could not discern the particles using phase contrast microscopy. We therefore functionalised the beads with AlexaFluor-488 Cadaverin (A30676, ThermoFisher) using the protocol described by Vorselen *et al.* [13]. The fluorescent beads were imaged using spinning disk confocal microscope with a 40× Plan Neufluar NA 1.30 oil objective. Figure 4.2 shows the distribution of size for the different samples. The table below shows the bead radii obtained and the

corresponding critical pressure for extrusion.

Cross Linker%	Sample	$P_{extrusion}$ (kPa)	Radius (μm)
2.3%	1	8	7.3 ± 1.1
	2	12	14 ± 4
1.5%	1	10	12 ± 4
	2	16	17 ± 5
1%	1	23	17 ± 6

The results show that for a pore size of 3.1 μm most of the samples have mean radii between 7 to 17 μm. The sizes are consistent with the typical sizes of human fibroblast cells which have a radius $\sim$ 10 to $\sim$ 25 μm [19, 20]
The size of the particles is determined by the pore size and the pressure ($P_{extrusion}$) for extrusion. We observe that for the same cross-linker percentage an increase in extrusion pressure results in a larger bead radius and a larger standard deviation. We also observe that for a decrease in cross-linker percentage there is an increase in bead radius which is consistent with the results shown by Vorselen *et al.*[13]. However, for the 2.3% sample 1, 3% span80 was used along with AIBN concentration of 1.1 mg/mL while for sample 2, 1% span80 was used along with an AIBN concentration of 1.5 mg/mL. An increase in span80 concentration leads to an decrease in interfacial tension between the n-hexane and water interface [21]. The critical pressure depends on the interfacial tension as below:

$$P_{critical} = \frac{4\gamma \cos\theta}{D} \tag{4.1}$$

where, γ is the interfacial tension, θ is the angle of opening of the pores and D is the pore diameter. Therefore a decrease in the span80 concentration leads to a decrease in critical pressure and extrusion pressure which results in smaller size of the beads. An increase in AIBN concentration, on the other hand causes an increase in size of the micro-particles as was shown by Saadat *et al.* for methacrylic particles [22]. For the 2.3% sample, it is difficult to determine which effect causes an increase in bead radius. For the 1.5% sample, the AIBN and span80 concentrations are identical for the two samples and an increase in extrusion pressure alone seems to cause an increase the size of the beads. More experiments need to be done to determine the effect of pressure on the size of the beads.

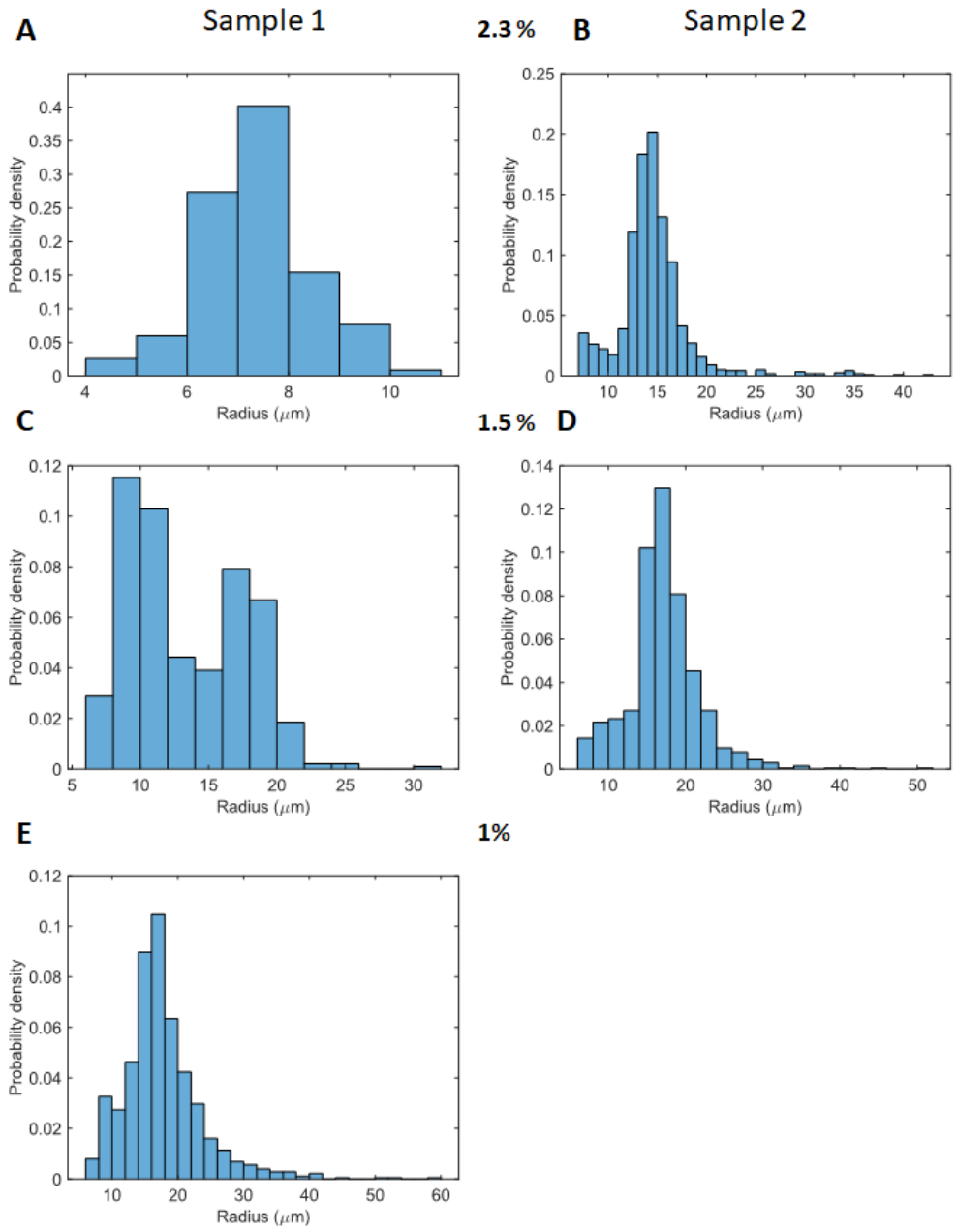

Figure 4.2: Mean radius of bead varies from 7-17 μm.
Size distribution of two different samples for 2.3, 1.5 and 1% cross linker concentration. ***A)-B)*** *2.3% cross linker. Sample 1 was imaged using fluorescently labelled particles on spinning disk confocal microscope.* ***C)-D)*** *1.5% cross linker.* ***E)*** *1% cross linker.*

4.3 Young's Modulus Depends on Size

Next, we measured the Young's Modulus of the synthesised beads. Each sample was fixed on 2 different plates and measured independently on the AFM. Figure 4.3 shows the plot of Young's modulus versus size of the beads. The two different measurements on each sample are shown in red and blue. The overlapping regions of the two measurements were used to perform the T-test to determine whether the two measurements came from the same distribution and if they could be combined. For Figure 4.3A, B and C the corresponding p-values from the T-test were 0.90, 0.30 and 0.29. Since the p-value was greater than 0.05, this suggested for the three samples we could combine the two measurements. For 1.5% sample in Figure 4.3D the data followed a trend however the p-value obtained from the t-test was 0.04. Therefore this suggested that the two measurements could not be combined. For the purposes of the results, we analysed just the first measurement for the sample in Figure 4.3D. For Figure 4.3E the overlapping region was very small to get a statistically accurate t-test. However, there was a clear trend in Young's modulus as the size increases and the two data measurements moved into each other and therefore we chose to combine the two measurements for the 1% sample. We then calculated the correlation coefficient for each sample. The table below shows the correlation coefficients for the different samples.

Cross Linker%	Sample	Young's Modulus (Pa)	Correlation Coefficient
2.3%	1 2	50-300 100-1200	-0.4422 -0.6043
1.5%	1 2	400-1200 200-1200	-0.6762 -0.7485
1%	1	100-1000	-0.8302

The results show that there is a strong negative correlation between the measured Young's modulus and the size of the bead measured. We also see that the Young's modulus measured ranges from 100 Pa to 1200 Pa across the 5 samples. The measured Young's modulus is in range with the cell stiffness measured using AFM by Cross *et al.* where they showed that tumour cells have a stiffness in the range of 0.53 kPa while benign cells have a stiffness of 1.97 kPa [23]. Similar study on epithelial cancer cells was done by Li *et al.* which showed cancerous epithelial cells were 1.5 times softer than normal epithelial cells with Young's modulus of 0.39 kPa

while normal cells have a Young's modulus of 0.54 kPa [24].

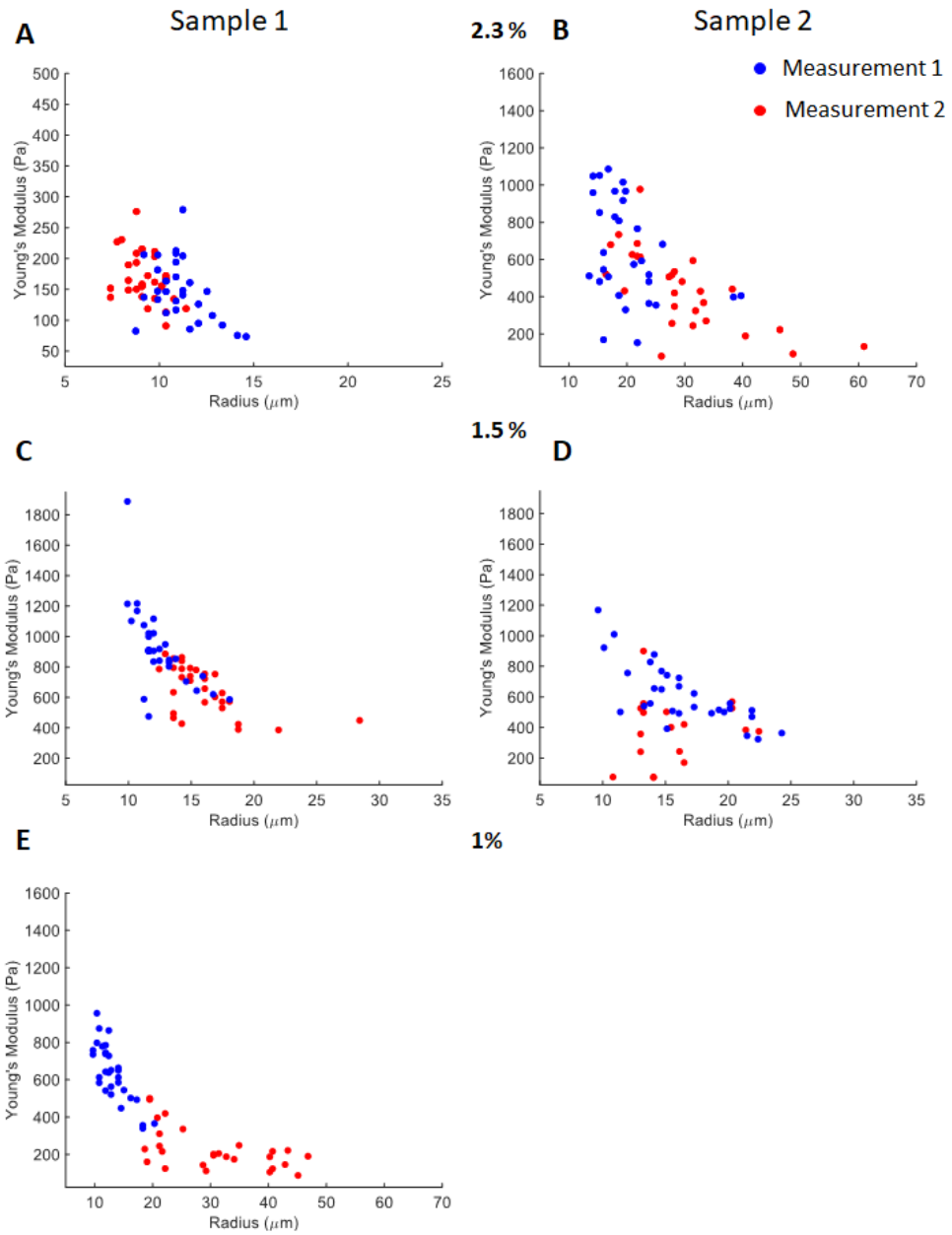

Figure 4.3: Young's Modulus shows a negative correlation with the size of the bead.
Each sample was independently measured two times. All samples show a negative correlation with the size of the bead. ***A)-B)*** *2.3% cross linker.* ***C)-D)*** *1.5% cross linker.* ***E)*** *1% cross linker.*

Further, we wanted to investigate how the Young's modulus depends on size of the particle. For this purpose, we plotted the data on a log-log scale and fitted a linear equation (y=mx+c) to get the slope. Figure 4.4 shows the data for the five samples. We see that the data follows a straight line with a slope of ~ -1 as shown in the table below:

Cross Linker%	Sample	Fitted Slope	R^2
2.3%	1	-1.0 $\pm$ 0.5	0.2219
	2	-1.1 $\pm$ 0.4	0.3705
1.5%	1	-1.2 $\pm$ 0.3	0.5622
	2	-1.0 $\pm$ 0.3	0.5838
1%	1	-1.23 $\pm$ 0.16	0.8042

Here, the R^2 value signifies the goodness of the fit and gives the fraction of the data follows the fit. The result suggests that the effective Young's modulus of the bead depends on the radius of the bead as $\sim \frac{1}{R}$ irrespective of the cross linker concentration.

Version of August 19, 2021– Created August 19, 2021 - 15:19

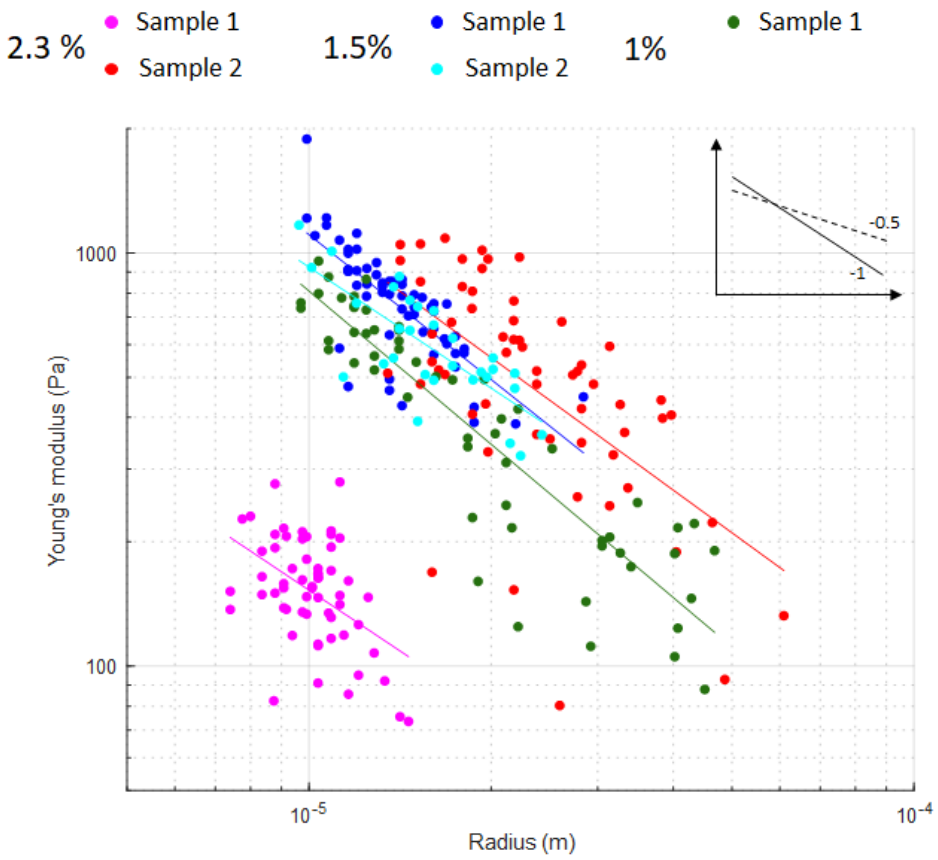

Figure 4.4: Effective Young's modulus shows a $\frac{1}{R_S}$ with the size of the particle. *All samples irrespective of the cross linker percentage show a $\frac{1}{R_S}$ dependence. The data on the log-log plot is fitted to y=mx+c. (inset) shows the curves with slope -1 (solid) and -0.5 (dashed). -0.5 slope decays slower than the data shown in the figure. As the cross linker percentage decreases the stiffness also decreases as can be seen from the downward movement of the respective samples. 2.3% Sample 1 does not follow this trend as it has less AIBN concentration (1.1 mg/mL) compared to the other samples (1.5 mg/mL). This fitting can be used as a calibration curve to determine Young's modulus of beads of all sizes within a sample.*

We see that as the cross linker concentration decreases the stiffness also decreases as expected. The 2.3% sample 1 (shown in magenta) has a lower stiffness than 2.3% sample 2 (shown in red) because we used a lower concentration of AIBN. The 2.3% sample 1 also shows a lower R^2 value compared to the other samples as the size distribution is very homogeneous which makes it difficult to fit a linear curve to the data. The sample also shows a lower magnitude of correlation coefficient. This suggests that for

a homogeneous size distribution the trend is not significant and one can directly determine the mean Young's modulus. For sample 2 of 1.5% cross linker we plot only the first measurement and discard the second. This is reasonable as the second measurement does not represent the sample. We believe so because the dish used for the second measurement was stored for three weeks before measurement whereas the rest of the samples were measured within 4 days of fixing the beads. The beads optically look different on the AFM microscope as shown in supplementary Figure 6.1. It seems as if the sample collapsed after a long storage and a dent can be discerned in the centre of the bead. Another reason to disregard the second measurement was that we only measured Young's modulus on 18 beads as compared to 27-30 beads for the rest of the samples.
The samples do not follow the $\frac{1}{\sqrt{R}}$ relation as is shown in Equation 2.5. More experiments need to be done to determine the $\frac{1}{R}$ relation that we see in the samples. One of the possible reasons could be that the sample when indented deforms from the top and bottom instead of just the top as is assumed in the Hertzian model. Another reason could be that there is a dominating effect of the surface tension which could also cause the $\frac{1}{R}$ dependence of Young's modulus that we see. However, using such a fitting method we can form a calibration curve to determine the Young's moduli for all the beads for each sample. The pressure that can be measured follows a linear relation with the Young's modulus [15]. Experimental data demonstrates that the smallest pressure we can measure is $\sim$ 42 Pa using 1 kPa beads (unpublished work, Rick Rodrigues de Mercado, Schmidt Lab). Extrapolating the linear relation for the softest particles ($E_S \sim 175$ Pa) synthesised in this thesis, we can measure a pressure of ~ 7.3 Pa.

Chapter 5

Conclusion

In this thesis, we have characterised soft hydrogel beads for their size and stiffness. We have shown that we can make beads in the range of 7-17 μm in radius and Young's moduli ranging from 200-1200 Pa which are similar to cells and therefore an be used in tissues to mimic cells. We have also shown that the effective Young's modulus depends on the size of the bead as $\frac{1}{R_S}$.
The work in this thesis provides a novel insight on the size dependence of the effective Young's modulus of the beads. We can make a calibration curve for individual samples to determine Young's moduli of beads with different sizes in the sample. It also underlines the importance of having a sample with a homogeneous size distribution to get the mean Young's modulus of the sample. Once the size dependence of the beads is better understood this method provides a simple way to quickly synthesise a large number of beads of desired stiffness. From the softest beads synthesised with Young's modulus $\sim$ 175 Pa, the smallest pressure we can measure is $\sim$ 7.3 Pa.
These beads can be used for a variety of different force measurements. These beads can be coated with necessary proteins and embedded in tumour tissues to determine the effect of cellular forces on tumour metastasis. They can be used to probe cell-cell interactions in tissue and how cells achieve confluency.

Acknowledgement

I would like to thank Rick Rodrigues de Mercado for the assistance in the project, Prof. Dr. Thomas Schmidt for the critical inputs and Dr. Alexandre Morin for serving as the second corrector.

Chapter 6

Supplementary Figures

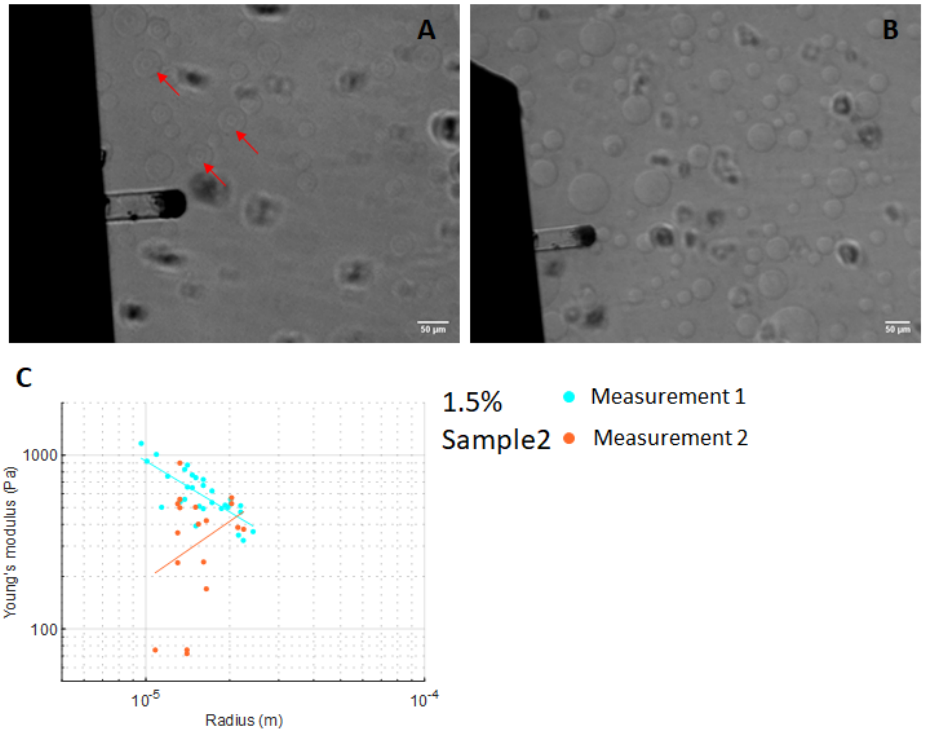

Figure 6.1: Beads from 1.5% sample 2 appear different from other samples and show an opposite trend.
A) *Image taken on the AFM microscope for 1.5% cross linker sample 2 shows a ring in the centre of the bead. This suggests that the integrity of the bead is lost and the bead may have collapsed.* ***B)*** *Image taken on the AFM microscope for 2.3% cross linker sample 2 does not show the ring in the centre of the bead.* ***C)*** *Young's modulus vs Radius plotted on the log-log scale for both measurements of the 1.5% sample. Measurement 2 has less number of data points and fit yields a slope of* 1.11 ± 1.87 *and an* R^2 *value of 0.09.*

Bibliography

[1] Kyle H Vining and David J Mooney. Mechanical forces direct stem cell behaviour in development and regeneration. *Nature reviews Molecular cell biology*, 18(12):728–742, 2017.

[2] Matteo Rauzi, Pascale Verant, Thomas Lecuit, and Pierre-François Lenne. Nature and anisotropy of cortical forces orienting drosophila tissue morphogenesis. *Nature cell biology*, 10(12):1401–1410, 2008.

[3] M Tse Janet, Gang Cheng, James A Tyrrell, Sarah A Wilcox-Adelman, Yves Boucher, Rakesh K Jain, and Lance L Munn. Mechanical compression drives cancer cells toward invasive phenotype. *Proceedings of the National Academy of Sciences*, 109(3):911–916, 2012.

[4] Armen H Mekhdjian, FuiBoon Kai, Matthew G Rubashkin, Louis S Prahl, Laralynne M Przybyla, Alexandra L McGregor, Emily S Bell, J Matthew Barnes, Christopher C DuFort, Guanqing Ou, et al. Integrin-mediated traction force enhances paxillin molecular associations and adhesion dynamics that increase the invasiveness of tumor cells into a three-dimensional extracellular matrix. *Molecular biology of the cell*, 28(11):1467–1488, 2017.

[5] Andrew E Pelling and Michael A Horton. An historical perspective on cell mechanics. *Pflügers Archiv-European Journal of Physiology*, 456(1):3–12, 2008.

[6] Jochen Guck and Edwin R Chilvers. Mechanics meets medicine. *Science Translational Medicine*, 5(212):212fs41–212fs41, 2013.

[7] Sergey V Plotnikov, Ana M Pasapera, Benedikt Sabass, and Clare M Waterman. Force fluctuations within focal adhesions mediate ecm-

rigidity sensing to guide directed cell migration. *Cell*, 151(7):1513–1527, 2012.

[8] John L Tan, Joe Tien, Dana M Pirone, Darren S Gray, Kiran Bhadriraju, and Christopher S Chen. Cells lying on a bed of microneedles: an approach to isolate mechanical force. *Proceedings of the National Academy of Sciences*, 100(4):1484–1489, 2003.

[9] Hedde van Hoorn, Rolf Harkes, Ewa M Spiesz, Cornelis Storm, Danny van Noort, Benoit Ladoux, and Thomas Schmidt. The nanoscale architecture of force-bearing focal adhesions. *Nano letters*, 14(8):4257–4262, 2014.

[10] Robert M Hochmuth. Micropipette aspiration of living cells. *Journal of biomechanics*, 33(1):15–22, 2000.

[11] Otger Campàs, Tadanori Mammoto, Sean Hasso, Ralph A Sperling, Daniel O'connell, Ashley G Bischof, Richard Maas, David A Weitz, Lakshminarayanan Mahadevan, and Donald E Ingber. Quantifying cell-generated mechanical forces within living embryonic tissues. *Nature methods*, 11(2):183–189, 2014.

[12] Erfan Mohagheghian, Junyu Luo, Junjian Chen, Gaurav Chaudhary, Junwei Chen, Jian Sun, Randy H Ewoldt, and Ning Wang. Quantifying compressive forces between living cell layers and within tissues using elastic round microgels. *Nature communications*, 9(1):1–14, 2018.

[13] Daan Vorselen, Yifan Wang, Miguel M de Jesus, Pavak K Shah, Matthew J Footer, Morgan Huse, Wei Cai, and Julie A Theriot. Microparticle traction force microscopy reveals subcellular force exertion patterns in immune cell–target interactions. *Nature communications*, 11(1):1–14, 2020.

[14] Heinrich Rudolf Hertz. Uber die beruhrung fester elastischer korper und uber die harte. *Verhandlung des Vereins zur Beforderung des GewerbefleiBes, Berlin*, page 449, 1882.

[15] Valentin L Popov, Markus Heß, and Emanuel Willert. *Handbook of contact mechanics: exact solutions of axisymmetric contact problems*. Springer Nature, 2019.

[16] Ian N Sneddon. The relation between load and penetration in the axisymmetric boussinesq problem for a punch of arbitrary profile. *International journal of engineering science*, 3(1):47–57, 1965.

[17] John Canny. A computational approach to edge detection. *IEEE Transactions on pattern analysis and machine intelligence*, (6):679–698, 1986.

[18] Fernand Meyer. Topographic distance and watershed lines. *Signal processing*, 38(1):113–125, 1994.

[19] Rob Phillips; Jane Kondev;Julie Theriot; Hernan Garcia. *Physical Biology of the Cell (2nd Edition)*. Garland Science, 2 edition, 2012.

[20] Eric P Vander, Arthur J.;Widmaier. *Vander's human physiology: the mechanisms of body function*. McGraw-Hill Education, 15 edition, 2019.

[21] Leena Johanna Peltonen and Jouko Yliruusi. Surface pressure, hysteresis, interfacial tension, and cmc of four sorbitan monoesters at water–air, water–hexane, and hexane–air interfaces. *Journal of colloid and interface science*, 227(1):1–6, 2000.

[22] Younes Saadat, Soleyman Hosseinzadeh, Faramarz Afshar-Taromi, Hormoz Eslami, and Samira Abdolbaghi. Generalizing the polymerization conditions for the production of monodisperse polymeric particles via dispersion polymerization. *Colloid and Polymer Science*, 291(4):937–944, 2013.

[23] Sarah E Cross, Yu-Sheng Jin, Jianyu Rao, and James K Gimzewski. Nanomechanical analysis of cells from cancer patients. *Nature nanotechnology*, 2(12):780–783, 2007.

[24] QS Li, Gabriel YH Lee, Choon Nam Ong, and Chwee T Lim. Afm indentation study of breast cancer cells. *Biochemical and biophysical research communications*, 374(4):609–613, 2008.